Efficient sliding locomotion of three-link bodies with inertia

Adam Earnst* and Silas Alben†

Department of Mathematics, University of Michigan, Ann Arbor, MI 48109, USA

(Dated: July 23, 2021)

Inspired by the movement of snakes, this project focuses on the sliding locomotion of three-link bodies in the presence of Coulomb friction. Using Newton's second law, we create a system of differential equations that a sliding body must satisfy. With these equations as a constraint, we use a genetic optimization algorithm to find periodic single harmonic angle functions with respect to time that maximize the efficiency of the sliding body in different frictional regimes. Notably, we include inertia in our model, meaning that the period of motion can be any positive value, instead of being constrained to $T \to \infty$.

I. INTRODUCTION

In this work, we build upon previous results in [1], using the same three-link model that simplifies smooth body models such as in [2]. The benefit of our 3-link model is that it reduces the degrees of freedom of the body, allowing us to better investigate the full range of possible motions. Still, this model is able to approximate undulatory motions that are very common in swimming and crawling motion [3, 4]. In this paper, we will add non-negligible inertia to the model in [1], allowing us to consider larger body accelerations and quicker motions than before.

II. MODEL

We use the same Coulomb-friction model as [2, 5, 6] and other recent studies. The body is thin compared to its length, so for simplicity we approximate its motion by that of a polygonal curve $\mathbf{X}(s,t) = (x(s,t), y(s,t))$, parametrized by arc length s and varying with time t. A schematic diagram is shown in figure 1A.

The basic problem is to prescribe the time-dependent shape of the body in order to obtain efficient locomotion. The shape is described by $\Delta\theta_1(t)$ and $\Delta\theta_2(t)$, the differences between the tangent angles of the adjacent links. A set of possible body shapes is plotted at the corresponding $(\Delta\theta_1, \Delta\theta_2)$ locations in figure 1B. The region inside the gray polygonal boundary consists of shapes that do not self-intersect. Five examples of shapes that lie on the boundary are shown in red (along the upper right portion of the boundary). In this work we will consider time-periodic kinematics, which are represented by closed curves in the $(\Delta\theta_1, \Delta\theta_2)$-plane.

To write the dynamical equations (Newton's laws), we first write the body tangent angle as $\theta(s,t)$; it satisfies

*Electronic address: aearnst@umich.edu

†Electronic address: alben@umich.edu

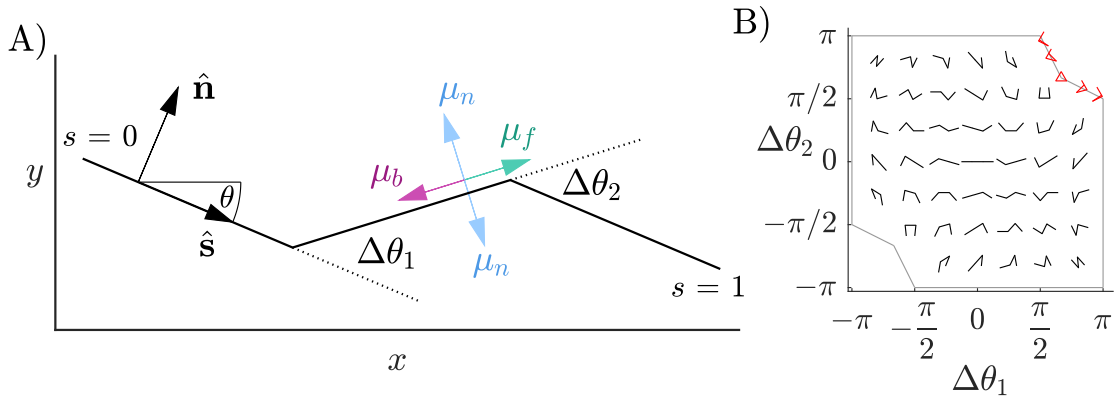

FIG. 1: A) Schematic diagram of a three-link body with changes in angles $\Delta\theta_1$ (here positive) and $\Delta\theta_2$ (here negative) between the links. The body is parametrized by arc length s (nondimensionalized by body length), at an instant in time. The tangent angle and the unit vectors tangent and normal to the curve at a point are labeled. Vectors representing forward, backward, and normal velocities are shown with the corresponding friction coefficients μ_f, μ_b, and μ_n. B) Examples of body shapes in the $(\Delta\theta_1, \Delta\theta_2)$-plane. Shapes that do not self-intersect are shown in black; a few shapes at the threshold of self-intersection are shown in red.

$\partial_s x = \cos\theta$ and $\partial_s y = \sin\theta$. The unit vectors tangent and normal to the body are $\hat{\mathbf{s}} = (\partial_s x, \partial_s y)$ and $\hat{\mathbf{n}} = (-\partial_s y, \partial_s x)$ respectively. We write

$$\theta(s,t) = \theta_0(t) + \Delta\theta_1(t)H(s-1/3) + \Delta\theta_2(t)H(s-2/3) \tag{1}$$

where H is the Heaviside function and $\theta_0(t)$ is the tangent angle at the "tail" (the $s = 0$ end), an unknown to be solved for using Newton's equations of motion. The body position is obtained by integrating θ:

$$x(s,t) = x_0(t) + \int_0^s \cos\theta(s',t)ds', \tag{2}$$

$$y(s,t) = y_0(t) + \int_0^s \sin\theta(s',t)ds'. \tag{3}$$

The tail position $\mathbf{X}_0(t) = (x_0(t), y_0(t))$ and tangent angle $\theta_0(t)$ are determined by the force and torque balance for the body, i.e. Newton's second law [2, 5]:

$$\int_0^L \rho\partial_{tt}x ds = \int_0^L f_x ds, \tag{4}$$

$$\int_0^L \rho\partial_{tt}y ds = \int_0^L f_y ds, \tag{5}$$

$$\int_0^L \rho\mathbf{X}^\perp \cdot \partial_{tt}\mathbf{X} ds = \int_0^L \mathbf{X}^\perp \cdot \mathbf{f} ds. \tag{6}$$

Here L is the body length, ρ is the body's mass per unit length, and $\mathbf{X}^\perp = (-y, x)$. For simplicity, the body is assumed to be locally inextensible so L is constant in time. $\mathbf{f}$ is the force per unit length on the body due to Coulomb friction with the ground:

$$\mathbf{f}(s,t) \equiv -\rho g\mu_n \left(\widehat{\partial_t\mathbf{X}_\delta} \cdot \hat{\mathbf{n}}\right)\hat{\mathbf{n}} - \rho g\left(\mu_f H(\widehat{\partial_t\mathbf{X}_\delta} \cdot \hat{\mathbf{s}}) + \mu_b(1 - H(\widehat{\partial_t\mathbf{X}_\delta} \cdot \hat{\mathbf{s}}))\right)\left(\widehat{\partial_t\mathbf{X}_\delta} \cdot \hat{\mathbf{s}}\right)\hat{\mathbf{s}}, \tag{7}$$

$$\widehat{\partial_t\mathbf{X}_\delta} \equiv \frac{(\partial_t x, \partial_t y)}{\sqrt{\partial_t x^2 + \partial_t y^2 + \delta^2}}, \tag{8}$$

and g is gravitational acceleration. Again H is the Heaviside function, and $\widehat{\partial_t \mathbf{X}}_\delta$ is the normalized velocity, regularized with a small parameter $\delta = 10^{-3}$ here. Nonzero δ avoids nonsolvability of the equations in a small number of cases where static friction comes into play, but δ has little effect on the solutions as long as it is much smaller than the scale of body velocities (typically $O(1)$), as detailed in [1] in the isotropic case. We find empirically that there is little change in the results (less than 1% in relative magnitude) when δ is decreased below 10^{-3}.

According to (7) the body experiences friction with different coefficients for motions in different directions with respect to the body. The frictional coefficients are μ_f, μ_b, and μ_n for motions in the forward ($\hat{\mathbf{s}}$), backward ($-\hat{\mathbf{s}}$), and normal ($\pm\hat{\mathbf{n}}$) directions, respectively. If $\mu_b \neq \mu_f$, we define the forward direction so that $\mu_f < \mu_b$, without loss of generality. In general the body velocity at a given point has both tangential and normal components, and the frictional force density has components acting in each direction. A similar decomposition of force into directional components occurs for viscous fluid forces on slender bodies [7].

We nondimensionalize equations (4)–(6) by dividing lengths by the body length L and mass by ρL. We nondimensionalize the time t by $\sqrt{L/g}$, and assume that the body shape $(\Delta\theta_1(t), \Delta\theta_2(t))$ is periodic in time (as is typical for steady locomotion [5]) with dimensionless period T. We compute the motions with respect to a time variable $\tau = t/T$, the time scaled by the period, so that a population of motions with different periods can be computed as an ensemble on the same τ grid. Using τ, the dimensionless equations (4)–(6) are

$$\frac{1}{T^2}\int_0^1 \partial_{\tau\tau} x ds = \int_0^1 f_x ds, \tag{9}$$

$$\frac{1}{T^2}\int_0^1 \partial_{\tau\tau} y ds = \int_0^1 f_y ds, \tag{10}$$

$$\frac{1}{T^2}\int_0^1 \mathbf{X}^\perp \cdot \partial_{\tau\tau}\mathbf{X} ds = \int_0^1 \mathbf{X}^\perp \cdot \mathbf{f} ds. \tag{11}$$

In (9)–(11) and from now on, all variables are dimensionless. If we divide by μ_f in each of (9)–(11), we see the problem depends on three parameters: $1/\mu_f T^2$, μ_b/μ_f, and μ_n/μ_f.

When $(\Delta\theta_1(\tau), \Delta\theta_2(\tau))$ is periodic, the body motion may be solved as an initial value problem by giving initial conditions for $\{x_0(\tau), y_0(\tau), \theta_0(\tau), \dot{x}_0(\tau), \dot{y}_0(\tau), \dot{\theta}_0(\tau)\}$ (all set to zero here), and then evolving them forward in time using (9)–(11). We find that generically the resulting body motion $\mathbf{X}(s,\tau)$ evolves towards a time-periodic state with the same τ period (1) as $(\Delta\theta_1(\tau), \Delta\theta_2(t\tau))$. In this state, the body undergoes nonzero net rotation after each period, and over long times it traces out a circular path in the $x-y$ plane. Therefore the time-averaged speed of the body is zero unless there is zero net rotation. Part of our definition of locomotor efficiency is the body's average speed—i.e. the magnitude of the average velocity of the body's center of mass—over a finite time interval of length T_1 starting at time t_0 (with corresponding τ values τ_0 and $\mathcal{T}_1$):

$$\|\langle\overline{\partial_t \mathbf{X}}\rangle\| \equiv \left\| \frac{1}{T_1}\int_{t_0}^{t_0+T_1}\int_0^1 \partial_t \mathbf{X}\, ds\, dt \right\| \tag{12}$$

$$= \frac{1}{T_1}\sqrt{\left(\int_0^1 x(s,t_0+T_1) - x(s,t_0) ds\right)^2 + \left(\int_0^1 y(s,t_0+T_1) - y(s,t_0) ds\right)^2} \tag{13}$$

$$= \frac{1}{T_1}\sqrt{\left(\int_0^1 x(s,\tau_0+\mathcal{T}_1) - x(s,\tau_0) ds\right)^2 + \left(\int_0^1 y(s,\tau_0+\mathcal{T}_1) - y(s,\tau_0) ds\right)^2}. \tag{14}$$

With large $\mathcal{T}_1$ we approximate the long-time average, but since $\mathcal{T}_1$ is finite, motions with nonzero rotation can achieve nonzero, and possibly large, average speeds. A typical measure of efficiency [2, 5, 6, 8] is

$$\lambda = \frac{\|\langle\overline{\partial_t \mathbf{X}}\rangle\|}{\langle P\rangle}, \tag{15}$$

the ratio of the average speed with the average power

$$\langle P\rangle = \frac{1}{T_1}\int_{t_0}^{t_0+T_1}\int_0^1 -\mathbf{f}(s,t)\cdot\partial_t\mathbf{X}(s,t)\,ds\,dt = \frac{1}{\mathcal{T}_1}\int_{\tau_0}^{\tau_0+\mathcal{T}_1}\int_0^1 -\mathbf{f}(s,\tau)\cdot\partial_\tau\mathbf{X}(s,\tau)\,ds\,d\tau \tag{16}$$

Both $\langle P\rangle$ and $\|\langle\overline{\partial_t \mathbf{X}}\rangle\|$ scale with velocity, but their ratio λ does not. Nonetheless, the solutions depend on the period of motion since it sets the magnitudes of the left hand sides (inertia terms) in (9)–(11), so λ does vary with the period of the body kinematics $(\Delta\theta_1(t), \Delta\theta_2(t))$, though not as a simple scaling law.

The upper bound on efficiency is

$$\lambda_{ub} = \frac{1}{\min(\mu_f, \mu_b, \mu_n)}, \tag{17}$$

corresponding to uniform motion in the direction of least friction, and can be approached by a sequence of particular concertina-like motions, as shown in [1]. In this work we take the relative efficiency λ/λ_{ub} as the primary measure of performance.

III. SINGLE-HARMONIC (ELLIPTICAL) KINEMATICS

We begin by considering body kinematics given by a single harmonic, corresponding to elliptical trajectories in the $(\Delta\theta_1, \Delta\theta_2)$-plane:

$$\Delta\theta_1(t) = A_{10} + A_{11}\cos(2\pi t) + B_{11}\sin(2\pi t), \quad \Delta\theta_2(t) = A_{20} + A_{21}\cos(2\pi t) + B_{21}\sin(2\pi t), \quad 0 \le t \le 1. \tag{18}$$

An example is the gray ellipse in figure 2A, with the coefficient values shown as vectors.

As in previous works [9, 10], we pay particular attention to the subset of paths that yield no net rotation of the body over one cycle, because these are the kinematics that yield nonzero net locomotion over a long-time average. If there is a nonzero net rotation, points on the body move along circles over large times, so the long-time average velocity is zero. However, such kinematics could still yield efficient locomotion over short-to-medium times, particularly if the net rotation is small. We consider this possibility later. In [1] we showed that if we neglect inertia, no net rotation occurs for paths that have a certain bilateral symmetry, under reflection in the line $\Delta\theta_1 = -\Delta\theta_2$, e.g. the blue ellipse in panel B. In that work we discussed the case $\mu_b = \mu_f$, but the same argument holds if $\mu_b \neq \mu_f$. The rotation that occurs as the body traverses the half-ellipse above the line $\Delta\theta_1 = -\Delta\theta_2$ is cancelled by the rotation that occurs on the half-ellipse below the line. Ellipses with bilateral symmetry can be parametrized as

$$\Delta\theta_1(t) = A_0 + A_1\cos(2\pi t) + B_1\sin(2\pi t), \quad \Delta\theta_2(t) = -A_0 - A_1\cos(2\pi t) + B_1\sin(2\pi t), \quad 0 \le t \le 1. \tag{19}$$

with only three parameters versus six (counting the phase) for general ellipses. We may take $A_1 \ge 0$ without loss of generality, by shifting $t \to t + 1/2$ if necessary, which leaves the path unchanged. For motions with no net rotation, this change of phase does not change the displacement or efficiency.

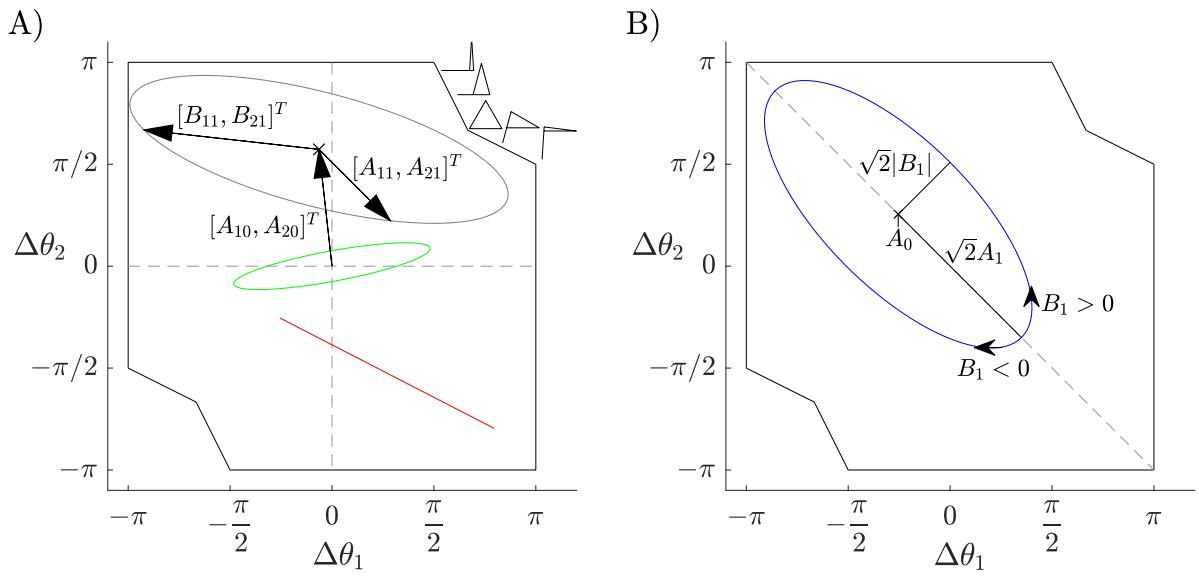

FIG. 2: A) Examples of elliptical trajectories in the region of non-self-intersecting configurations (inside the black polygonal outline). Examples of body configurations at the boundary of the region are shown at upper right. The gray ellipse has center A_{10}, A_{20} and shape given by $\{A_{11}, A_{21}, B_{11}, B_{21}\}$. B) $(\Delta\theta_1(t), \Delta\theta_2(t))$ for a three-link body, symmetric about the line $\Delta\theta_1 = -\Delta\theta_2$. A_0 is the average of $\Delta\theta_1$ over the ellipse and $\sqrt{2}A_1$ and $\sqrt{2}|B_1|$ are the semi-major and semi-minor axes of the ellipse. The sign of B_1 gives the direction in which the path is traversed.

Another set of paths that yield no net rotation in the inertia-free case are those with antipodal symmetry, i.e. symmetry with respect to reflection in the origin, such as the green ellipse in panel A. In this case, the body rotations at antipodal points cancel, and the net rotation over a full path is zero. Ellipses with antipodal symmetry are also parametrized by three parameters

$$\Delta\theta_1(t) = A_{11}\cos(2\pi t) + B_{11}\sin(2\pi t), \quad \Delta\theta_2(t) = -A_{11}\cos(2\pi t) + B_{21}\sin(2\pi t), \quad 0 \le t \le 1. \tag{20}$$

where A_{21} has again been set to $-A_{11}$ to fix the arbitrary phase.

The lack of net rotation for trajectories with bilateral and antipodal symmetry was also shown by [11]. A third special case that we discuss later is reciprocal kinematics—kinematics that are the same under time reversal. These are degenerate ellipses that reduce to straight line segments, e.g. the red line in panel A. These yield no net locomotion if $\mu_b = \mu_f$ but can yield efficient locomotion in other cases.

IV. RESULTS

A. Efficient single-harmonic kinematics

When we consider non-negligible inertia, we are unable to exploit the same bilateral symmetries as in [1], as these trajectories no longer necessarily result in zero rotational speed. Thus, we expand the set of all possible single-harmonic trajectories in the $(\Delta\theta_1, \Delta\theta_2)$-plane to include all possible ellipses as described by (18). We can re-express

equation (18) as follows; I provide the intermediate steps only for $\Delta\theta_1$:

$$\Delta\theta_1(t) = A_{10} + A_{11}\cos(2\pi t) + B_{11}\sin(2\pi t) = A_{10} + \sqrt{A_{11}^2 + B_{11}^2}\left(\frac{A_{11}}{\sqrt{A_{11}^2 + B_{11}^2}}\cos(2\pi t) + \frac{B_{11}}{\sqrt{A_{11}^2 + B_{11}^2}}\sin(2\pi t)\right) \tag{21}$$

$$= A_{10} + \sqrt{A_{11}^2 + B_{11}^2}\left(\cos(\phi_1)\cos(2\pi t) + \sin(\phi_1)\sin(2\pi t)\right) \tag{22}$$

$$= A_{10} + \sqrt{A_{11}^2 + B_{11}^2}\cos(2\pi t - \phi_1) \tag{23}$$

for some angle $\phi_1 \in [0, 2\pi)$. Similarly,

$$\Delta\theta_2(t) = A_{20} + \sqrt{A_{21}^2 + B_{21}^2}\cos(2\pi t - \phi_2) \tag{24}$$

It is clear that in the interval $0 \leq t \leq 1$, the global extrema of $\Delta\theta_1$ and $\Delta\theta_2$ are $A_{10} \pm \sqrt{A_{11}^2 + B_{11}^2}$ and $A_{20} \pm \sqrt{A_{21}^2 + B_{21}^2}$, respectively. For the absolute value of these extrema to not exceed π, we must have that

$$\sqrt{A_{11}^2 + B_{11}^2} < \pi - |A_{10}|, \ \sqrt{A_{21}^2 + B_{21}^2} < \pi - |A_{20}|, \tag{25}$$

To make sure that the absolute values of the link angles do not exceed π, which would correspond to one type of self-intersection, we select Fourier coefficients that satisfy equation (25). We do this by first assigning A_{10} and A_{20} random values in the interval $(-\pi, \pi)$. Then, we assign random values to A_{11} and A_{21} such that $|A_{11}| < \pi - |A_{10}|$ and $|A_{21}| < \pi - |A_{20}|$. Finally, we assign random values to B_{11} and B_{21} such that $|B_{11}| < \sqrt{(\pi - |A_{10}|)^2 - A_{11}^2}$ and $|B_{21}| < \sqrt{(\pi - |A_{20}|)^2 - A_{21}^2}$, so that equation (25) is satisfied. Our only other optimization parameter is $\rho = 1/\mu_f T^2$, which we let range from 10^{-3} to 10^2.

We optimize the relative efficiency λ/λ_{ub} over the set of all possible coefficients determined in this fashion, using a genetic optimization algorithm. In this algorithm, we create a population of 50 individual trajectories, defined by the Fourier coefficients in (18) and a value of ρ. For each iteration, we choose the top 50% of trajectories in terms of efficiency, and add random perturbations to the parameters for those trajectories, drawn from a uniform distribution. We repeat this process for many generations, and stop after the maximum efficiency in the population stagnates (increases by less than 0.001 in 20 generations). Then, if different populations converged to different optima, we select the population with the highest maximum efficiency.

We perform this process for various friction coefficient ratios $(\mu_n/\mu_f, \mu_b/\mu_f)$ ranging over a 12-by-8 grid with values shown on the axes of figure 3A. After all 96 optima were found, a k-means clustering algorithm was used to differentiate 10 clusters of optima, denoted by different colors in figure 3. In figure 3A, each square corresponding to a $(\mu_n/\mu_f, \mu_b/\mu_f)$ pair is given a different color, corresponding to the optimal elliptical trajectory in that case. Panel B plots an example elliptical trajectory for each of the 10 types of optima. The arrows denote the direction of motion of each elliptical trajectory.

Panel A shows us that like in [1], the clusters appear in contiguous regions in $(\mu_n/\mu_f, \mu_b/\mu_f)$ space. However, there still were some difficulties in classifying the elliptical trajectories. Namely, when $\mu_n/\mu_f < 1$, the characteristic ellipses for each cluster are very similar. This meant that based on different initial points for the k-means algorithm, the borders of each cluster varied slightly. Nonetheless, it is still possible to classify the optima based on 7 regions in $(\mu_n/\mu_f, \mu_b/\mu_f)$ space:

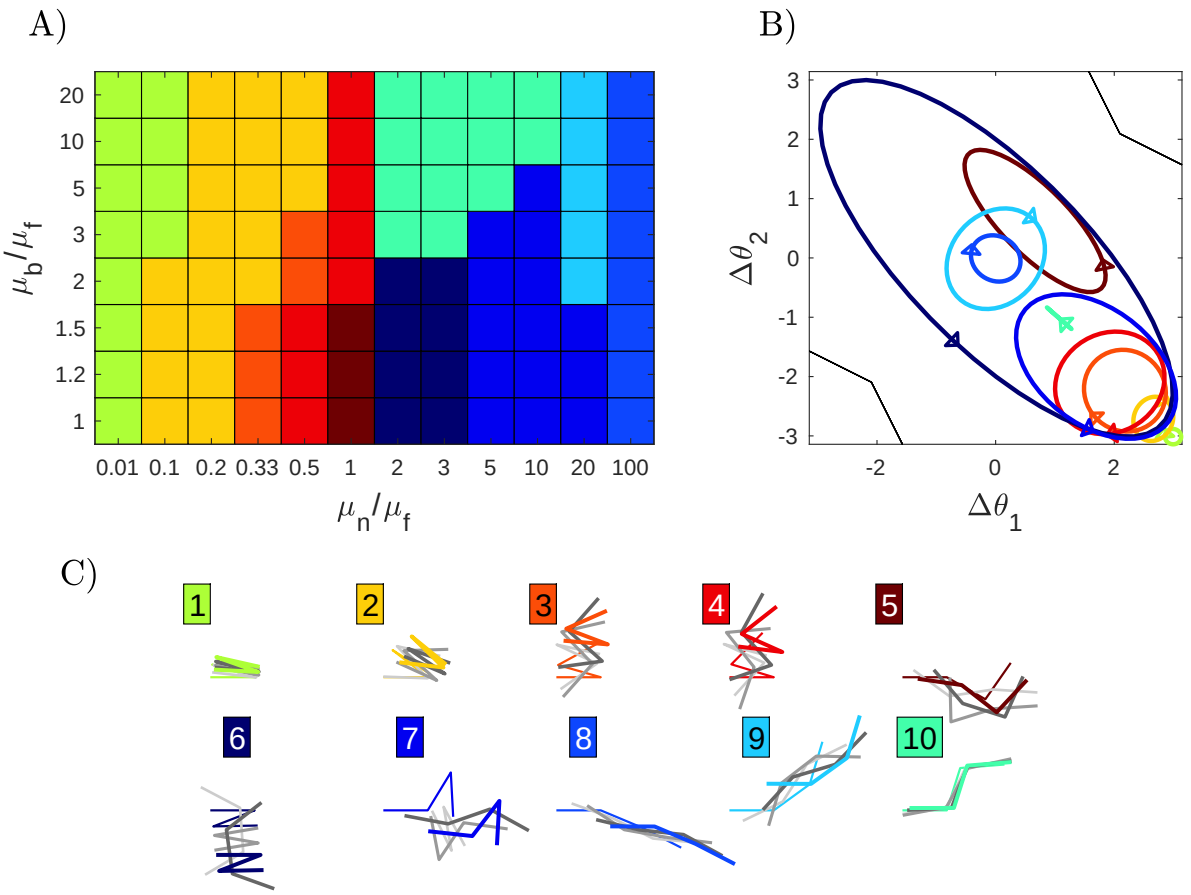

FIG. 3: A) Cluster classification of optimal elliptical trajectories over a $(\mu_n/\mu_f, \mu_b/\mu_f)$ grid. All of these global optima are partitioned into 10 groups based on their shape. The color of each square corresponds to the cluster to which an optimum value belongs. B) Characteristic elliptical trajectories for each of the 10 clusters. Arrows represent the direction of motion for each trajectory. C) Snapshots of the three-link body at five instants spaced 1/4-period apart. This progression of snapshots starts with the thin colored line, proceeds from light to dark gray, finishing with the thick colored line.

1. $\mu_n/\mu_f \ll 1$, represented by optima 1 and 2 (numbered in panel C). These optima are small amplitude oscillations in which $\Delta\theta_1$ and $\Delta\theta_2$ are always large in magnitude, meaning that the body is folded together.

2. $\mu_n/\mu_f < 1$ but not $\ll 1$ and $\mu_n/\mu_f = 1, \mu_b/\mu_f > 1$, represented by optima 3 and 4. These optima have larger amplitude oscillations than 1 and 2, but are similar in that the signs of $\Delta\theta_1$ and $\Delta\theta_2$ never change, and the body is mostly folded up.

3. $\mu_n/\mu_f = 1, \mu_b/\mu_f \approx 1$, represented by optimum 5. This optimum is not bilaterally symmetric, unlike the others, which are roughly bilaterally symmetric. The movement of this optimum is undulating, with a medium-sized amplitude.

4. $\mu_n/\mu_f > 1, \mu_b/\mu_f \geq 1$, but not $\gg 1$, dominated by optimum 6. This motion has the largest amplitude of all 10 optima types.

5. $3 < \mu_n/\mu_f < 100$, with μ_b/μ_f not $\gg 1$, represented by optimum 8. Of all of the optima, this one most closely resembles concertina motion, with the body folding together before straightening out in each period.

6. $\mu_n/\mu_f > 1$ but not $\gg 1$, $\mu_b/\mu_f \gg 1$, dominated by optimum 10. This optimum has the smallest amplitude, excluding optimum 1.

7. $\mu_n/\mu_f \gg 1$, represented by optima 9 and 10. These optima are centered about $(\Delta\theta_1, \Delta\theta_2) = (0, 0)$, and have fairly small amplitudes, meaning that the body is generally unfolded in these cases.

Looking at the 10 clusters of optima and comparing to [1], it appears that considering inertia results in more optimal motions being centered about a nonzero point in $(\Delta\theta_1, \Delta\theta_2)$ space, meaning that these shapes are generally folded to a large extent. Of these optima, the most similar are optima 1, 2, 3, and 4. These optima are all centered about very folded configurations and have progressively larger amplitudes. When $\mu_n/\mu_f < 1$, the optima always lie in one of these clusters, going from small to large amplitude as μ_n/μ_f increases. The only optima that oscillate about the origin are 6, 8, and 9. These motions are only optimal in select cases where $\mu_n/\mu_f > 1$.

The only one of our optimization parameters that is not represented in the elliptical trajectories is $\rho = 1/\mu_f T^2$. We represent this in figure 4, which shows the optimal value of ρ for each optimum found earlier. We can split $(\mu_n/\mu_f, \mu_b/\mu_f)$-space into four regions based on the optimal value of ρ:

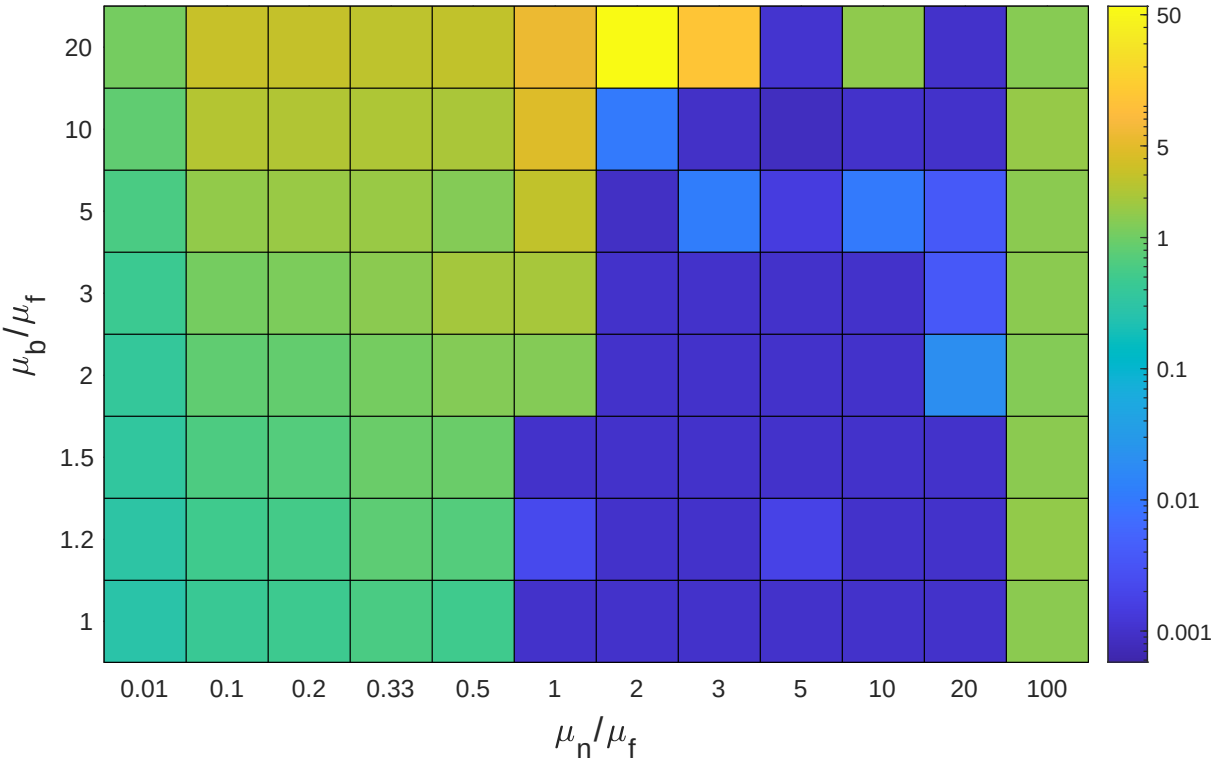

FIG. 4: Values of $\rho = 1/\mu_f T^2$ for each optimum at various points in $(\mu_n/\mu_f, \mu_b/\mu_f)$-space.

1. $\mu_n/\mu_f < 1$: ρ values are moderate ($0.1 < \rho < 5$) in this range, which aligns very closely with the regions of space where optima 1, 2, 3, and 4 (from figure 3) are found.

2. $\mu_n/\mu_f \approx 1, \mu_b/\mu_f \gg 1$: ρ values are very high ($5 < \rho < 60$) in this region.

3. $1 < \mu_n/\mu_f < 100$: ρ values are very small in this region ($0.001 < \rho < 0.1$), and often are equal to the set lower bound of 10^{-3}.

4. $\mu_n/\mu_f = 100$: ρ values are moderate in this region ($1 < \rho < 5$), which corresponds to optimum 8 in figure 3.

These four regions based on ρ show that the optimal value of ρ depends mainly on μ_n/μ_f. Each of the four regions, with the exception of region 2, only depends on the value of μ_n/μ_f. Region 2 is also unique because the values of ρ are significantly higher than anywhere else in $(\mu_n/\mu_f, \mu_b/\mu_f)$-space, exceeding 50 at $(\mu_n/\mu_f, \mu_b/\mu_f) = (2, 20)$. Another notable region is region 3, in which most values of ρ are very close to 10^{-3}, our lower bound. This lower bound was not decreased to 0, because the numerical approach used to calculate the three-body-link's motion did not always converge in those cases. However, since 10^{-3} is very small, it can be assumed that in this region, efficiency is optimized when $\rho \approx 0$, corresponding to the inertia-free case investigated in [1].

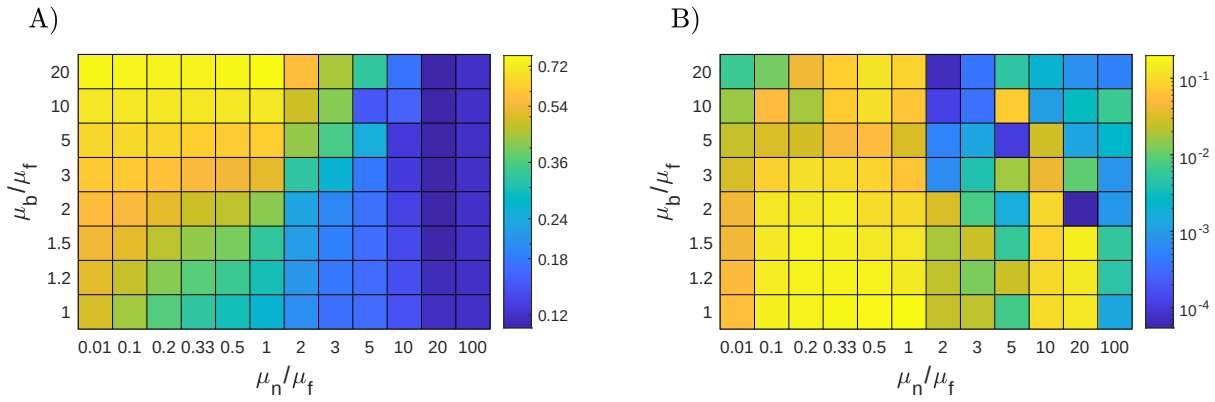

FIG. 5: A) Relative efficiencies λ/λ_{ub} for global optima among elliptical trajectories. B) Absolute values of the mean rotational speeds of the optimal trajectories, as defined in equation (26).

Figure 5A shows the relative efficiencies of the global optima over $(\mu_n/\mu_f, \mu_b/\mu_f)$-space. The maximum efficiency, approximately 0.78, occurs at $(\mu_n/\mu_f, \mu_b/\mu_f) = (1, 20)$, the same as the best optimum in figure [1]. This motion is characterized by motion 4 in 3C. In general, λ/λ_{ub} increases when μ_n/μ_f decreases and μ_b/μ_f increases. This results in a cluster of efficiencies near 0.7 when $\mu_n/\mu_f < 1, \mu_b/\mu_f \gg 1$. In contrast, when $\mu_n/\mu_f \gg 1$, the relative efficiencies of the optimal motions are much lower, around 0.12.

In figure 5B, we look at the mean rotational speeds of the optimal trajectories. We measure this rotational speed using the equation

$$\omega = \frac{1}{\mathcal{T}_1}\left(\theta_0(\tau_0 + \mathcal{T}_1) - \theta_0(\tau_0)\right) \tag{26}$$

This equation calculates the average rotation of the body over a period. Large values of ω mean that over many periods, the efficiency of the body will decrease. This is because the body will trace out a circular path in the $x-y$ plane, eventually returning to its initial position. Despite this, these optima can still yield efficient locomotion over shorter time-frames. Analyzing the mean rotational speeds of the optimal elliptical kinematics in panel B, it is evident that mean rotational speed is greatest when $\mu_n/\mu_f \leq 1$. These mean rotational speeds never exceed $0.2 \approx \frac{\pi}{16}$. When $\mu_n/\mu_f > 1$, more optima have very small mean rotational speeds. However, unlike many of the other quantities we have plotted, mean rotational speeds vary greatly even among nearby points in $(\mu_n/\mu_f, \mu_b/\mu_f)$-space, and it is difficult to see exactly how ω depends on μ_n/μ_f and μ_b/μ_f.

B. Isotropic friction

When the optimal single-harmonic kinematic trajectories were computed for many points in $(\mu_n/\mu_f, \mu_b/\mu_f)$-space, motion 5 in figure 3 was an obvious outlier, not displaying the same bilateral symmetry across the line $\Delta\theta_1 = -\Delta\theta_2$ as all of the other 9 motions. Instead, these motions have a different type of bilateral symmetry, under reflection in the line $\Delta\theta_1 = \Delta\theta_2$. We will call this bilateral persymmetry, as it resembles a persymmetric matrix, which is symmetric in the northeast to southwest diagonal. We can represent an elliptical bilateral persymmetric path using three parameters, and the equation closely resembles our typical bilateral symmetry:

$$\Delta\theta_1(t) = A_0 + A_1\cos(2\pi t) + B_1\sin(2\pi t), \quad \Delta\theta_2(t) = A_0 - A_1\cos(2\pi t) + B_1\sin(2\pi t), \quad 0 \leq t \leq 1. \tag{27}$$

To investigate this case further, we will take a deeper look at the case of isotropic friction, one of the cases in which the typical bilateral symmetry is not observed. In the inertia-free case ($\rho = 0$), it was found that the optimal motion was a large bilateral ellipse [1], shown by the red dashed ellipse in figure 6. To compare the case with inertia to the simpler inertia-free case, we set ρ at different constants and performed genetic optimization over the parameters A_0, A_1, and B_1. Figure 6A shows the optimal ellipses for different values of ρ ranging from 0.001 (the thickest line), to 100 (the thinnest line). The relative efficiency of these optimal motions increases as $\rho \to 0$, tending towards the inertia-free case. However, at no value of ρ does the optimal ellipse resemble that for the inertia-free case, the red dashed ellipse. To investigate further, we took the trajectories that were optimal for the various values of ρ and plotted their efficiencies over a range of ρ values. We then compared this to the behavior of the inertia-free optimum over the same range of ρ. This is plotted in 6B. This figure shows that although the inertia-free optimum has a high efficiency at small values of ρ, its efficiency decreases more drastically when ρ increases. Therefore, this bilateral elliptical trajectory is nearly optimal for $\rho \ll 1$, but when the period T decreases (causing ρ to increase), it is no longer efficient. With higher ρ, bilateral persymmetric ellipses dominate in efficiency.

Another factor to consider in the isotropic case is the mean rotational speed of the resulting 3-link body. When inertia was neglected, we could not guarantee that bilateral persymmetric ellipses would have zero net rotation, unlike with the typical bilateral ellipses symmetric in $\Delta\theta_1 = -\Delta\theta_2$. Figure 5B shows that in the isotropic case, $\omega \approx 0.2$, the largest of any trajectory in $(\mu_n/\mu_f, \mu_b/\mu_f)$-space. However, this rotational speed is not significantly different than the typical bilateral ellipses for $\mu_n/\mu_f < 1, \mu_b/\mu_f > 1$.

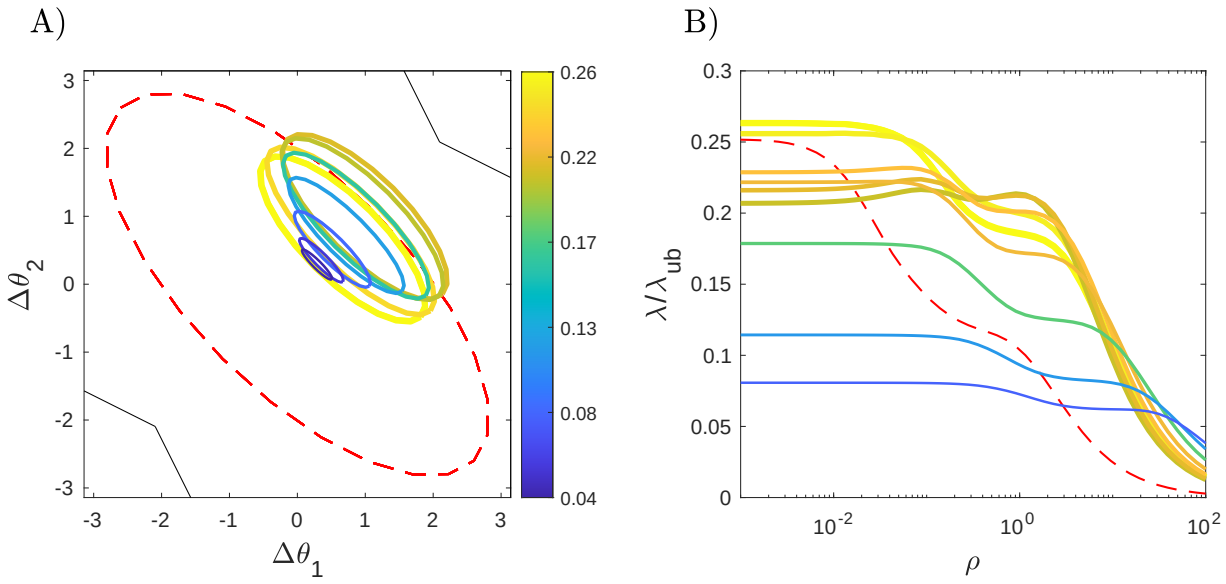

FIG. 6: A) Optimal elliptical trajectories for different values of $\rho = 1/\mu_f T^2$ in the isotropic case (when $\mu_n/\mu_f = \mu_b/\mu_f = 1$). The plotted ellipses maximize efficiency for each $\rho \in \{0.001, 0.01, 0.1, 1, 2, 5, 10, 20, 50, 100\}$. In the figure, these values are represented by the thickness of the ellipse - the lines range from the thickest for small ρ to the thinnest for large ρ. The color of each ellipse represents its relative efficiency, as shown on the colorbar. The red dashed ellipse represents the optimum for the inertia-free case with isotropic friction, found in [1]. B) A plot of efficiency for these optimal trajectories at different values of ρ. Each line corresponds to the ellipse of the same color.

V. SUMMARY AND CONCLUSIONS

In this paper, we have explored efficient single-harmonic kinematics of three-link body motion, both in anisotropic and isotropic cases. We were able to classify efficient motions in different regions of $(\mu_n/\mu_f, \mu_b/\mu_f)$-space, comparing some of the optima to those in the inertia-free case [1]. In the continuation of this project, we have several goals. First of all, we aim to expand the efficiency optimization problem to multiple-harmonic kinematics, by adding higher-frequency terms to our Fourier coefficients. Additionally, many of the efficient trajectories had very small amplitude oscillations, which resulted in a very low average speed. In some situations, it could be more useful to maximize distance traveled in a given period of time instead of efficiency. We aim to address this question, finding non-periodic trajectories that maximize the distance the body travels, and performing multi-objective optimization with efficiency and distance traveled as the two objective functions.

Acknowledgments

I would like to express my gratitude to the Department of Mathematics at the University of Michigan for making this REU project possible, and to my mentor, Silas Alben, for his guidance and assistance throughout the program.

This research was supported by the NSF Mathematical Biology program under award number DMS-1811889.

[1] Silas Alben. Efficient sliding locomotion with isotropic friction. *Physical Review E*, 99(6):062402, 2019.

[2] D L Hu and M Shelley. Slithering Locomotion. In *Natural Locomotion in Fluids and on Surfaces*, pages 117–135. Springer, 2012.

[3] Edward M Purcell. Life at low Reynolds number. *American journal of physics*, 45(1):3–11, 1977.

[4] Geoffrey Ingram Taylor. Analysis of the swimming of long and narrow animals. *Proc. R. Soc. Lond. A*, 214(1117):158–183, 1952.

[5] D L Hu, J Nirody, T Scott, and M J Shelley. The mechanics of slithering locomotion. *Proceedings of the National Academy of Sciences*, 106(25):10081, 2009.

[6] F Jing and S Alben. Optimization of two- and three-link snake-like locomotion. *Physical Review E*, 87(2):022711, 2013.

[7] RG Cox. The motion of long slender bodies in a viscous fluid. Part 1. General theory. *Journal of Fluid Mechanics*, 44(04):791–810, 1970.

[8] S Alben. Optimizing snake locomotion in the plane. *Proc. Roy. Soc. A*, 469(2159):1–28, 2013.

[9] D Tam and A E Hosoi. Optimal stroke patterns for Purcell's three-link swimmer. *Physical Review Letters*, 98(6):68105, 2007.

[10] François Alouges, Antonio DeSimone, Laetitia Giraldi, Yizhar Or, and Oren Wiezel. Energy-optimal strokes for multi-link microswimmers: Purcell's loops and Taylor's waves reconciled. *New Journal of Physics*, 21(4):043050, 2019.

[11] Emiliya Gutman and Yizhar Or. Symmetries and gaits for Purcell's three-link microswimmer model. *IEEE Transactions on Robotics*, 32(1):53–69, 2015.